PROCEEDINGS, 49th Workshop on Geothermal Reservoir Engineering
Stanford University, Stanford, California, February 12-14, 2024
SGP-TR-xxx

Deep Seismic Sensor Stimulation Wavefield Empirics for Ambient Crust Surface Seismic Flow Imaging

P. Leary[1], P. Malin[2], P. Geiser[3], C. Sicking[4]
[1]38 Beauchamp Ave, Royal Leamington Spa, Warwickshire, UK CV32 5TA
[1]peter@geoflowimaging.com; [2]malin@duke.edu, [3]peter.geiser@gmail.com, [4]charles@ambientreservoir.com

Keywords: EGS, stimulation microseismicity, crustal permeability, kHz seismic wavefields, seismic scattering, Arps hyperbolic distributions, Newberry Geothermal Field Seismic Emission Tomography imaging.

Two microearthquake (Meq) wavefield spectral and coda empirics recorded by 1.5-2.5km deep sensors at Enhanced Geothermal System (EGS) stimulation projects are key to achieving surface-sensor images of ambient crust fluid flow structures. First, deep crustal stimulation Meqs generate kHz wavelets not directly visible on surface seismic sensors. The observed Meq spectra $S_2(f) \sim 1/(1+[|(f-f_1)/f_0|]^p)$, $2 < p < 3$, $f_1 \sim 1$kHz, $f_0 \sim 200$Hz indicates that Meq source dislocations are multidirectional – radial/bidirectional rather than unidirectional – as opposed to fault-like planes having expected form $S_{1=1}(f) \sim 1/(1+(f/f_c)^p)$, $2 < p < 3$. Second, seismic scattering of these kHz stimulation wavelets generates persistent coda wavetrains with amplitudes declining hyperbolically rather than exponentially. Hyperbolic oil well production decline, as documented by Arps, logically implies that seismic scattering occurs via similarly distributed permeability structures. We also identify decaHz-limited Meq wavefields in the spectral range of surface seismic sensors. Scattered stimulation Meq emissions thus produce flow-field related seismic wavefields in surface sensor recordings. The Meq size-and-spatial correlations are congruent with the size-and-spatial correlation properties of ambient crust porosity and permeability, which are related by $\kappa(x,y,z) \sim \exp(\alpha\varphi(x,y,z))$. In this empirical relation $\varphi(x,y,z)$ represents the pink-noise porosity distributions found in well-log data worldwide. The poroperm-connectivity parameter α renders $\kappa(x,y,z)$ lognormal as attested by well-flow data worldwide: a few wells contribute the most production. The surface sensor wavefield data can be processed by Seismic Emission Tomography (SET) into images of subsurface flow structures with 20-40m spatial resolution. SET images enable (i) tracking of EGS stimulation enhancement and (ii) provide production well targets for improved drilling efficiency. We conclude our presentation with an example of SET flow structure imaging at the Newberry Geothermal Field.

Introduction

In the 1970s EGS stimulation of permeability by high pressure & volume fluid injection was viewed as producing stress-aligned planar fractures in a quasi-uniform elastic continuum with pore-fluids a largely secondary feature [1-4]. Quasi-uniform media allow regional stresses to align induced fractures that can connect injection and production wells over large offsets via planar Poiseuille ("cubic law") flow [5-8]. Associated EGS microseismic (Meq) emissions were thought to occur as slips on these stress-aligned fractures in close analogy to fault zone seismicity [9-11]. Such Meqs were taken to be largely randomly distributed among fluid-induced slip surfaces as modelled by discrete fracture networks (DFN) [11-14].

We here look at a range of km-deep seismic sensor EGS stimulation Meq waveform and related data. These give a distinctly different account of rock-fluid interactions in the ambient crust. The following deep seismic sensor observations are made:

(i) Meq emission waveforms occur at kHz rather than the decaHz frequencies inferred from surface sensor data;
(ii) Meq displacement waveform spectra in frequency f show a 2-parameter relation $S_2(f) \sim 1/(1+[|(f-f_1)/f_0|^p])$, $2 < p < 3$;
(iii) This is distinct from 1-parameter expression $S_1(f) \sim 1/(1+|f/f_c|^p)$ familiar from of fault-zone seismic studies [2].;
(iv) Meq coda wave amplitude declines are hyperbolic. $A(t) \sim 1/(1 + nt/t_0)^{1/n}$, $1 < n < 2$;
(v) This is distinct from the commonly assumed single-scale exponential, $A_X(t) \sim \exp(-t/t_0)$;
(vi) Hyperbolic coda declines parallel the decline of oil-field well production demonstrated by Arps 80 years ago [15].
(vii) Spectra of minute-long background wavefields contain decaHz energy not directly attributable to Meq emissions;
(viii) The observed spectral frequency parameter $f_c \sim 100$ pertains to Meqs of magnitude $m > 0$
(ix) Whereas the observed EGS stimulation Meq magnitudes are $m < 0$;
(x) The minute-long background wavefields at kHz frequencies are spatially coherent across multiple 10m offsets;
(xi) Minute-long background wavefields at decaHz frequencies are spatially coherent across multiple at 75m offsets;
(xii) Cross-sensor coherence of decaHz energy ascends through vertical array sensors at P-wave speeds;
(xiii) This reveals the existence of ascending decaHz scattered waves from stimulation volumes;
(xiv) These waves can be recorded by surface sensors and processed by Seismic Emission Topography (SET) [16-18].

Further, surface observations of Meq magnitudes and pairwise spatial correlations are statistically congruent with the size and pairwise spatial correlation distributions of ambient crust poro-permeability. This empiric poro-permeability is given by $\kappa(x,y,z) \sim \exp(\alpha\varphi(x,y,z)$ and has been derived from well-log, well-core and well-flow data observed worldwide [19-23].

From the deep and surface sensor data empirics, we conclude that standard EGS stimulation of the ambient crust proceeds by driving injection fluids into a pre-existing ambient crust poro-permeability field $\kappa(x,y,z) \sim \exp(\alpha\varphi(x,y,z))$. Such unstable over-

pressured poro-permeability structures rupture with emission of radially-directed seismic displacement wavefields at kHz frequencies. The largest of these poro-permeability structure emissions are recorded by band-limited surface sensor networks as standard Meq activity. But by the spectral empirics of deep sensor waveform data, only rarely if ever are these ruptures specific to faults or fault-like structures in the stimulation volume. Wholly novel, and far more meaningful to surface seismic sensor observation, are the observed ascending decaHz background scattered and residual emission wavefields that are generated within the stimulation volume and propagate to the surface. These scattered/residual decaHz wavefields are too low in amplitude and too disseminated in time to be recognised as distinct events on surface sensor records. They are, however, sufficiently localised/coherent in time and space to be identified statistically through the systematics of Seismic Emission Tomography (SET) multi-channel data processing [16-23].

The directly and indirectly observed empirics of kHz stimulation seismic wavefields as revealed by deep sensors extend the present-day standard fault-zone view of EGS and the equivalent seismic processes in the ambient crust. There is no wavefield evidence for EGS Meq emissions occurring as unidirectional slip on planar structures. Rather, evidence abounds for emissions from bidirectional source slip distributions that are logically attributable to radial dislocations. These dislocations are either towards or away from the sensor. Emissions from radial source slips towards a sensor arrive at the sensor before the arrival of emissions from radial source slips away from the sensor. The kHz frequencies seen on deep sensors are an order of magnitude higher than frequencies registered by surface sensors. Likewise, the decaHz motion seen in deep sensor wavefields are incompatible with emissions for fault-like slip events having magnitudes $m < 0$.

The following three sections describe the empirics of deep seismic sensor waveform data acquired at two EGS stimulation projects. (1) A single channel of scalar strain data from 1.4km depth registered emissions from 1.4 km deep sourcing at 200-400m offsets in Utah granites [24]. (2) Stimulation Meq data recorded at 2-2.5km depth from 6km deep emissions in Finnish crystalline basement [11]. We first discuss the Utah and Finnish emission waveforms and spectra, then analyse their coda wave decline in the context of ambient crust poro-permeability distributions. A final section discusses the decaHz stimulation background velocity wavefield passing through the Finland sensor array while ascending from the stimulation volume. Such decaHz scattered wavefields are seen as a means of flow imaging of ambient crustal reservoir volumes; a concluding section notes likely applications of flow imaging for EGS and convective geothermal systems conditioned by the spatial complexity of the multiscale ambient crust flow systems given by the poro-permeability empiric $\kappa(x,y,z) \sim \exp(\alpha\varphi(x,y,z))$ attested by well-log, well-core, and well-flow data worldwide.

As a demonstration of the ability of surface-sensor ambient seismic recording to produce geologically interpretable SET images in a hydrothermal system, we end our discussion with recently acquired data from the Newberry Geothermal Field.

§§1 Deep seismic sensor Meq waveforms with non-fault-plane spectral empiric $S(f) \sim 1/(1+|(f-f_1)/f_0|^p)$

Two EGS stimulation projects contribute 1.5-2.5 km-deep seismic sensor data to our study. The projects are the April 2022 US DoE Forge stimulation of ~1/8km^3 of central Utah granitic basement at 1.5km depth recorded over several days by a single channel of strain sensor data at 1.4km depth [24] and the June 2018 and May 2020 st1 Deep Heat stimulation of ~1km^3 of Finnish basement at 6km depth near Helsinki as recorded by a 30-channel vertical array of geophones at depths between 2km and 2.5km [11]. The Utah data were recorded at 4kHz, and Helsinki data at 2kHz. The deep sensor wavefield data samples shown below are extracts from continuous monitoring sequences of one-minute duration. The present data samples capture, respectively, 127 Meq events and 34 Meq events occurring within approximately one day of stimulation.

The primary waveform data features for the Utah/Helsinki stimulation Meqs are illustrated in Figs 1-2. Fig 1 (left) shows kHz frequency scalar strain motion for large and small Utah project simulation events against 1 minute of sensor background strain motion sampled at 4kHz. Fig 1 (right) expands the strain motion time axis to give waveform detail, in particular the large event strain waveform amplitude decline curve. Fig 2 (left) shows hHz velocity motion for a Helsinki project stimulation Meq event data window sampled at 2kHz, with boxed wavefield components indicated along the expanded time axis (right). The first box marks the background wavefield before the Meq P-wave arrival; the second box marks the P-wave motion before the S-wave arrival; the final box marks the coda wave decline following the S-wave. On the expanded time-axis scale, the Helsinki waveform has widely separated P- and S-wave arrivals, reflecting the 4km source-sensor offset (6km deep stimulation volume below the 2km deep sensor). Like the Utah event, the Helsinki event wave train has an extensive coda wave decline curve; after 1000 half-msec samples (= ½ second), the coda wave amplitude remains well over the sensor background amplitude ahead of the P-wave arrival.

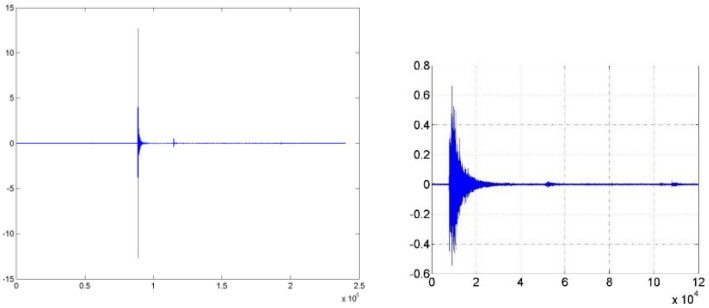

Fig 1 – (Left) One-minute Utah EGS stimulation data window of deep strain sensor with large and small Meq events sampled at 4kHz. (Right) Expanded time axis view of Meq strain displacement showing coda wave decline.

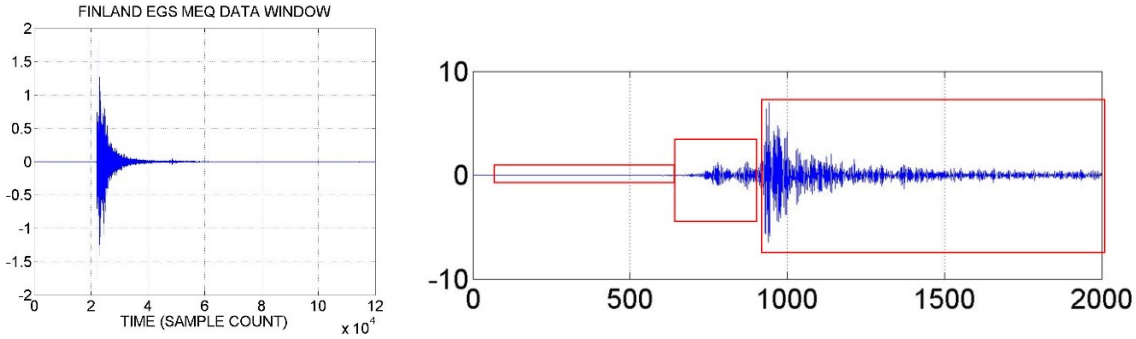

Fig 2-- (Left) One-minute Helsinki EGS stimulation data window of deep velocity sensor Meq event sampled at 2kHz. (Right) Expanded time axis view of Meq velocity showing pre-event background, P-wave arrival, and S-wave arrival with coda wave decline well above background for ½ second.

The characteristic frequency spectral content of the Utah and Helsinki deep sensor waveforms are given in Figs 3-4. Fig 3 shows the mean spectral distribution of 127 normalised Utah strain sensor waveform data windows such as illustrated in Fig 1; each data window was normalised to unit amplitude to avoid sample bias from a few large events. Three spectral features emerge in the blue spectral data trace. First, as expected from strain amplitudes present in Fig-1-like data windows, the spectral content is large at kHz frequencies. Second, not as expected, substantial strain amplitudes are present at decaHz frequencies. Third, also unexpected, kHz strain amplitude peaks are seen at a pair of frequencies. This pair of spectral peaks occurs at the same two frequencies for each event, and can thus be attributed to sensor instabilities. Sensor instability effects can be negated by digital filtering as given by the Fig 3 red trace.

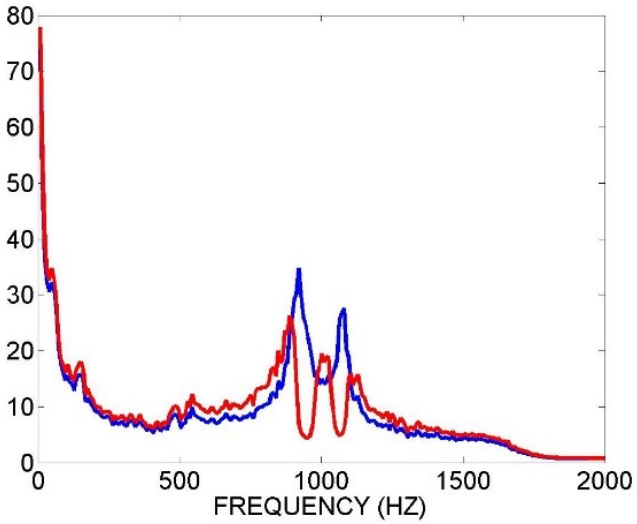

Fig 3 -- Mean Utah stimulation Meq strain wave frequency spectrum taken over 120 normalised events. Notable are (i) kHz central spectral energy, (ii) decaHz frequency spectral peak, and (iii) sharp spectral peaks in kHz range. The sharp wave spectral peaks occur at the same frequencies for all events, hence are sensor artifacts. Blue trace shows unfiltered data; red trace shows spike filtered data.

We now ask what is the nature of the unexpected decaHz spectral component? In the absence of the kHz spectral component, the decaHz spectral component would be attributed to Meq source slip mechanics. In light of the kHz spectral component, something is clearly going on. To answer this question, we look at the Helsinki site velocity waveform spectral data recorded at 4km offset from the EGS source volume.

Fig 4 shows four sample spectra for (left) 2- second background data intervals in advance of P-wave arrival, and (right red trace) 20-second intervals containing the data window Meq event. Fig 4 (left) is unlike Fig 3 in showing evidence of decaHz spectral amplitudes in background wavefields but with little evidence of kHz amplitudes. This feature is what would occur if the observed Fig 4 background wavefield were the result of systematic scattering loss of the Meq source wavelet kHz component. The Fig 4 decaHz wavefield is thus the residue of a scattering-depleted Meq source emission process observed at a large distance. In light of Fig 4 (left), we then interpret Fig 3 spectral components in terms of scattering over a limited source-sensor distance – 200-400m -- which leaves a more prominent Meq kHz spectral component relative to the decaHz scattered component. Fig 4 (right) fortifies the scattering process interpretation of Fig 3 and Fig 4 (left) by showing that the Fig 4 (left) spectral component in blue conforms in shape to Meq-specific spectra in red, i.e., Fig 4 (right) spectral traces in blue are the scattering residue of Meq-specific spectral traces in red.

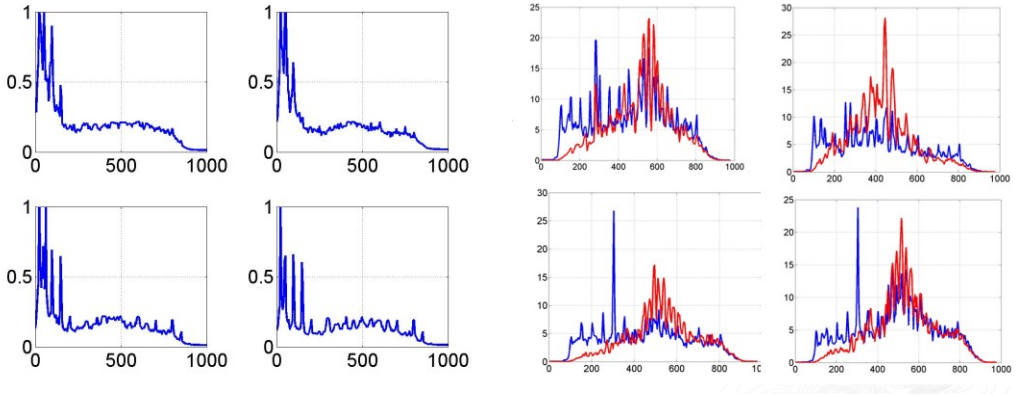

Fig 4 – (Left) Four samples of Helsinki stimulation Meq velocity sensor background wavefield spectra showing the presence of decaHz frequency energy as seen prominantly in Fig 3 Utah strain wave spectra. (Right) Same as (left) for foreground Meq data interval (red) with left-hand background spectra for frequencies above 100Hz adjusted to flanks of foreground spectra. These data show that the Helsinki background velocity wave fields are generated by stimulation Meq wavefields at hHz frequencies while at the same time have a decaHz component that is not part of the foreground spectra. We will see below that the decaHz spectral energy in both Utah and Helsinki stimulations arises from scattering processes and is thus not directly part of the Meq stimulation foreground process.

It is important to note that the highly scattered/attenuated low frequency spectral component of the Helsinki deep sensor background wavefield can be easily overlooked in relation to the large kHz P- and S-waves. The less scattered/attenuated decaHz frequency spectral component of Utah strain motion cannot be missed in the Utah deep sensor background wavefield. We thus establish prima facie case for kHz scattering processes that is independent of the coda wave amplitude declines phenomenology discussed in the following section.

Fig 5 presents the kHz/decaHz spectral systematics in a different format. We see Helsinki foreground/background spectral content collectively for a sample 60-second data window. The window is divided into 60 overlapping time slices, with the resulting spectra plotted for each time slice. For purposes of visual clarity, the spectral amplitudes plotted on the vertical axis are the square root of the actual amplitudes for the Meq interval time slices. It is seen that every time slice along the 60-second data window contains a steady level of decaHz wave amplitude. While only the Meq event time slices contain a dominant level of hHz wave amplitude, there is significant kHz wave amplitude in the trailing coda wave present in all 50 post-Meq time-slice windows. Most important, however, is that formally joining the Meq wave amplitudes are the decaHz wave amplitudes. Fig 5 makes clear that the Helsinki deep sensor background wavefield has a systematic physical presence of decaHz amplitudes that are logically due to seismic wave scattering from kHz Meq emission wavelets. We may remark here that there is little doubt that if

the Helsinki deep sensor data were sampled at 4hKz instead of 2kHz the high frequency spectral content would be in the kHz range in the Utah deep sensor data.

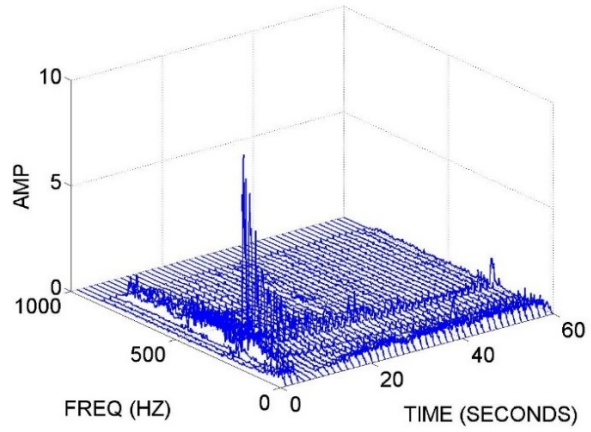

Fig 5 -- Spectral distribution of Helsinki deep sensor velocity wavefield time slices across a 1-minute time window such as Fig 2 (left). Of special note is the steady sequence of decaHz spectral amplitudes for all time slices, particularly those before the hHz spectral peaks from the embedded Meq emission waveform (the plotted decaHz amplitude decline for the Meq waveform time interval is an artefact of reduced hHz spectral peaks for visual clarity). The pre-Meq decaHz spectral amplitudes show that decaHz wave amplitudes are not a direct part of the Meq emission; by contrast, the sequence of hHz special amplitudes at times > 15 seconds arise from scattered coda waves trailing the Meq wavelet through the sensor array.

We now put the Utah/Helsinki deep seismic sensor wavefield spectral distributions illustrated by Figs 3-5 into the context of Meq dislocation slip mechanics. The connection between displacement sensor motion and source dislocation slip processes is given by Haskell's elastodynamics expressions [25-26]. Limiting ourselves to a single P-wave component of far-field displacement u at a fixed source sensor offset r and fixed angle relative to source dislocation slip velocities $\mathring{\Delta}_n(t)$ at time t, the Haskell solution reduces to $u(t + r/v) \sim S_n \mathring{\Delta}_n(t)$, v = P-wave velocity and S_n denotes summation of all source point dislocations that occur at source time t. . That is, Meq source dislocation movements of velocity $\mathring{\Delta}_n$ at time t collectively propagate at wave speed v to the sensor at distance r from the source to create displacement u at time $t + t/v$. It follows from Haskell's electrodynamic solution that the spectral content of observed far-field sensor displacement is determined by the dislocation slip motion of the Meq source. As such, the spectral content of the displacement sensor motion $u(t)$ places severe constraints of the dislocation slip motion giving rise to stimulation Meq wavelets accurately recorded by deep sensors.

It is well established that basic fault-zone dislocation slip takes place as an effective step-function in time [26]. From a state of zero motion, Meq dislocation slip proceeds along a fault-plane until it slows and stops. The corresponding far-field displacement likewise begins at zero, advances while the Meq slip advances, then abates as the source slip abates, with the final sensor displacement having a finite net value sensor displacement commensurate with the source finite dislocation final state. The overall frequency spectral content of displacement sensor motion is thus that of a step-function spectrum, $S_1(f) \sim 1/f$ [27]. The finite spatial dimension of the source slip plane ℓ enters into the sensor spectral distribution as internal interference which suppresses source emissions for frequencies above the characteristic value $f_c \sim v/\ell$. Together these low- and high - frequency wave processes are captured by the long-standing fault-zone spectral $S_1(f) \sim 1/(1+(f/f_c)^p)$, $2 < p < 3$ [9].

We have seen from deep seismic sensor data that Meq seismic waves are emitted at kHz frequencies that are not recorded by standard surface sensors. Meq dislocation slip mechanics based on decaHz-range surface sensor data are necessarily flawed. In particular, we see in Fig 6 that the standard approximation to fault-zone Meq displacement wavefield motion spectra $S_1(f) \sim 1/(1+(f/f_c)^p)$ shown in black traces is badly out of synch with the observed high frequency displacement wavefield emissions. The model-data mismatch holds for any value of the notional corner frequency f_c for exponents in the standard range $2 < p < 3$. Much more plausible is the red trace spectral empiric $S_2(f) \sim 1/(1+[|(f-f_1)/f_0|]^p)$ for the accepted exponent range $2 < p < 3$ with parameter values of central frequency $f_1 \sim 1$kHz and spectral width $f_0 \sim 200$Hz. The different central frequencies f_1 between the Utah strain sensor spectral data (left) and Helsinki spectral data (right) is plausibly attributed to the different sensor data sample rates (4kHz for Utah data, 2kHz for Helsinki data).

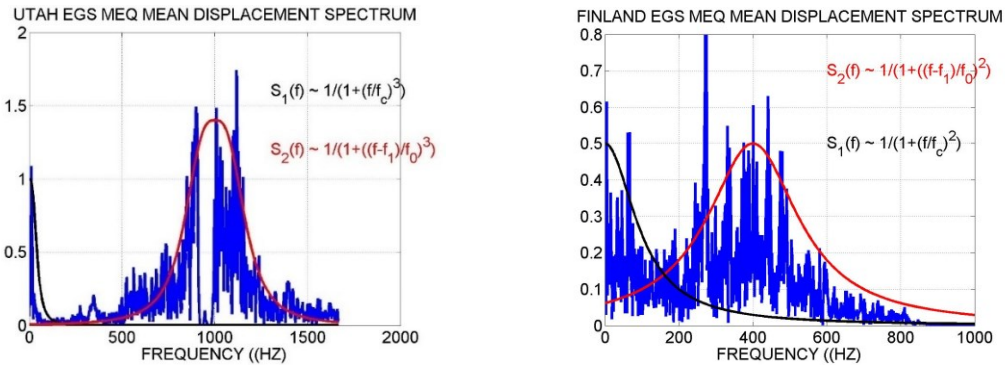

Fig 6 -- Stimulation Meq displacement waveform mean spectra (blue) for (left) 4kHz sampled Utah deep sensor data and (right) 2jHz sampled Helsinki deep sensor data, with empirical spectral distributions S_2 (red) and S_1 (black). The central frequency $f_1 \sim$ 1kHz distinguishes the S_2 form from the S_1 derived from fault-zone seismicity. It follows that the Utah and Helsinki stimulation Meq source dislocation slips do not occur on fault-like fracture structures. The low frequency spectral content traced by the black S1 spectral form is due to low frequency scattered wavefields recorded by the deep sensors; the corner frequency parameter values 50Hz < f_c < 100Hz for the black traces correspond to fault-zone slip events of magnitudes $m > 0$, inconsistent with the corner frequency range for event magnitudes $m < 0$, notionally assigned to the stimulation Meqs.

` Fig 7 synopsises the Fig 6 displacement sensor spectral distributions S_1 and S_2 for the EGS stimulation Meq source emission dislocation slip distributions. Displacement spectra S_1 with finite low frequency values and vanishing high frequency values plotted at upper left are associated with step-function-like source emission dislocations as plotted at upper right. In contrast, displacement spectra S_2 with finite central frequency values and vanishing low frequency value at lower left s is associated with rapidly fluctuating boxcar-like source emission dislocation slip distributions at lower right. The unidirectional step function source slip is the long-recognised character of fault-zone Meq slip motion]…]. Bidirectional fluctuation source slip motion that has not heretofore been recognised in surface seismic sensor data is plausibly attributed to radially directed motion driven by an expanding over-pressured fluid within spatially complex poro-permeability structures stimulated by EGS fluid injection. The inherent bidirectionality of source emission slips pictured in Fig 7 lower right comes from radially directed dislocations. Emissions from source dislocation slips towards a sensor from source points closer to the sensor arrive at the sensor before the arrivals of emissions from source slips away from the sensor.

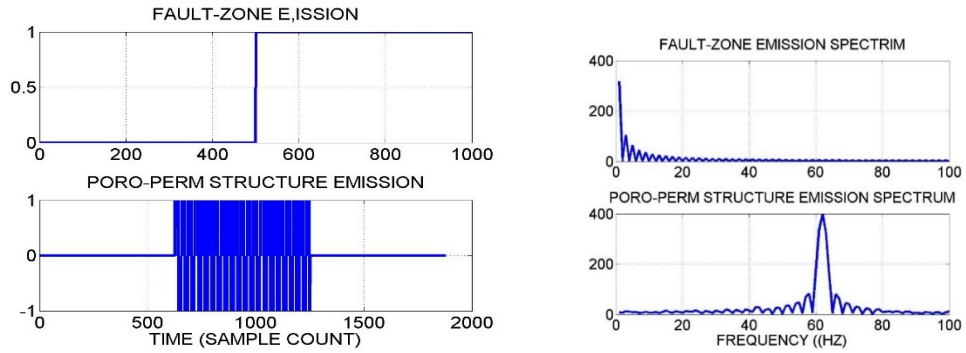

Fig 7 -- (Left) Type displacement waveforms for fault-zone dislocation slip (upper) and poro-permeability structure radial dislocation slip (lower). (Right) Type displacement slip waveform spectra for fault-zone slip (upper) and poro-permeability structure radial slip (lower).

Fig 9 sketches the sensor waveform effect of radial source slip motion. The scale of the central frequency of such sensor displacement motion is set by the dimension of the poro-permeability structure ℓ and P-wave velocity v_P, $f_1 \sim v_P/\ell$, where v_P ~5500m/s. For characteristic poro-permeability structure dimension $\ell \sim$ 5m the characteristic delay between source motions toward and away from the sensor is $\delta t \sim \ell/v_P$, setting the observed spectral central frequency ay $f_1 \sim$ 1kHz.

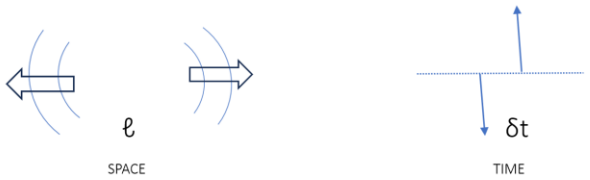

Fig 8 -- (Left) Radial source dislocation slip motion at source time *t* of fluid expanding from overpressured poro-permeability structure of dimension ℓ. (Right) Displacement sensor signals at sensor times *t* + *r*/*c* and *t* + *r*/*c* + *δt* from l radial source dislocation slip; earlier/downward signal emanates from right-pointing dislocation slip and later/upward signal emanates from left-pointing dislocation slip at time delay *δt* = ℓ/c', where *c* and *c'* are respectively the P-wave speed and the fluid rupture speed, and *r* is the source-sensor offset.

As a further Meq spectral consideration. we note here that the S_2 central spectral frequency $f_1 \sim 1$kNz cannot be logically interpreted as a fault-zone planar surface corner frequency associated with a fault of dimension $\ell \sim 5$m. As seen in Fig 9, fault-zone emission corner frequencies of order $f_c \sim 1$kHz are plotted for Meq moments $M \sim 10^7$N-m. From the standard moment-magnitude relation $m \sim (\log_{10}M - 9)/1.5$, moments $M \sim 10^7$N-m are equivalent to the magnitude $m < 0$ notionally assigned to Utah/Helsinki stimulation Meqs. However, by Fig 9, the $S_1(f)$ corner frequency interference process applied to fault planes is spectrally distributed over the 100-1000Hz frequency passband. By Fig 6, the black $S_1(f)$ spectral traces rule out fault-plane corner-frequency interference for frequencies above $f_c < 100$Hz. While some degree of inconsistency between Utah/Helsinki deep sensor waveform spectra and fault-zone slip mechanics might be expected, the next section shows that Fig 6 decaHz frequency spectral values are traced to background scattered wavefields emission wavefields.

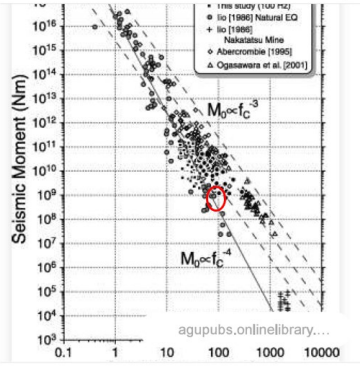

Fig 9 -- The power-law scaling of standard fault-zone dislocation slip corner frequency f_c as a function of earthquake moment *M*. The red circle indicates the range of corner frequencies $f_c \sim 100$Hz associated with magnitude $m \sim 0$ as given by the standard relation $m \sim (\log_{10}M - 9)/1.5$ [28]. For fault-zone slip Meqs of magnitude range $-2 < m < -1$ assigned to Utah and Helsinki stimulation events, the expected comer frequencies are of order f ~ 1000Hz ($10^6 < M < 10^{7.5}$), an order of magnitude greater than permitted by Figs 3-4, 6 observation.

§3§2 -- Deep sensor Meq emission coda hyperbolic decline as seismic scattering by ambient poro-permeability structures

In addition to kHz Meq seismic emission data for EGS crustal stimulation, Figs 1-2 illustrate a second fundamental feature of deep sensor data not evident in band-limited surface seismic records. Visible in both Utah and Finland stimulation waveforms are prolonged emission wave amplitude declines over several thousand samples before disappearing into the long term background seismic noise. While the Meq emission spectra are similar for the Utah and Finland sites, the respective Fig 1-2 one-minute data windows show that the extended post-P-/S-wave arrivals have extended coda wavetrains of different duration. Coda wave durations are much greater for the Helsinki site than for the Utah site. As noted earlier, this is difference in coda duration is arises from the order of magnitude greater source-sensor travel distance: 4km for Helsinki versus ~200-400m for Utah. Duration aside, however. the two projects exhibit the same coda amplitude decline empirics.

Fig 10 illustrates the distinctive feature of deep sensor coda data. As in all non-uniform seismic media, P- and S-waves traveling directly from source to sensor are followed in time by seismic waves that has been deviated, or scattered, from the direct path. The coda wave amplitude decline detail provided by deep sensors is critical in that Fig 10 Meq coda wave durations are seen to be substantially longer than the exponential decline of standard crustal scattering analyses [29].

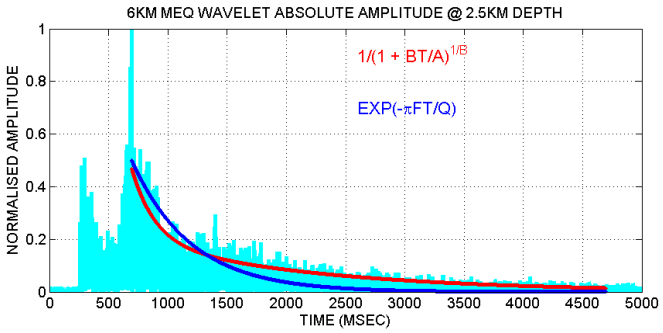

Fig 10 -Helsinki Meq coda wave amplitude decline matched to exponential (blue) and hyperbolic (red) curves. Compared with the hyperbolic curve, the exponential curve fails to match the data at low and high elapsed times.

Standard accounts of crustal seismic wave scattering are based on acoustic wave scattering in the atmosphere and ocean [30]. Acoustic wave scattering in primarily uniform media allows for a single characteristic inhomogeneity scale length ξ by which to retard traveling waves at comparable wavelengths, $2\pi\xi/\lambda \sim 1$. Such πscattering attenuation is commonly expressed as an exponential function of travel path r $A(r) \sim \exp(-\pi r/Q\xi)$, with quality factor Q measuring the scattering removal of energy from the Meq emission wavelet [29]. Expressed in n time, wavelet amplitude decline is $A(t) \sim \exp(-t/t_0)$, $t_0 = Q\xi/\pi v$. For media with little intrinsic attenuation losing wave energy to heat, all scattered wave energy is delayed behind the primary pulse to form the coda wave train. In the deep sensor coda wavetrain data in Fig 10 we see that the single scale length exponential attenuation decline does not match the observed amplitude decline extended duration. Something is going on in the crustal scattering process that is not going on in atmospheric/oceanic media.

That something else was first encountered some 80 years ago by Arps, who empirically derived the hyperbolic decline curve $A_H(t) \sim 1/(1 + nt/t_0)^{1/n}$, $1 < n < 2$,that allows for the systematic presence of multiple scales of flow structure in crustal reservoirs. Fig 10 shows that the Arps phenomenology applies to crustal scattering. We observe coda wave amplitude decline which provides both an accurate description of varied deep sensor Meq high frequency scattering coda eaves, and at the same time provides logical link to the multiscale ambient crust poro-permeability spatial distribution $\kappa(x,y,z) \sim \exp(\alpha\varphi(x,y,z))$. As summarised in Fig 14 below, the multiscale nature of crustal flow was not recognised as such by Arps but is now seen above as fundamental to the fluid-rock interaction in the ambient crust.

Fig 11 quickly surveys the empirics of our deep sensor Meq coda multiscale phenomenology. First, the red curve establishes the standard/normative picture of scattered wave amplitude decline as a function of elapsed time t, $A(t=r/c) \sim \exp(-\pi tc/Q\xi)$ for c = seismic wave speed. Such exponential declines posit as single scale length ξ and quality factor Q. The blue curve in Fig 11 is a particular case of the Arps hyperbolic curve $H(t) \sim 1/(1 + b't/t_0)^{1/b'}$, $1 < b' < 2$. that allows for multiscale processes. For numerical purposes, it is convenient to use the parameter $b' = 1 + b$ in relation to the Arps parameter b expressed below; e.g., Arps evaluation $b \sim 0.5$ equates to our parameter $b' = 1.5$. The blue hyperbolic curve with $b' = 1$ closely approximates the exponential decline in red that corresponds to the Arps condition $b = 0$. Key to Fig 11 are the black hyperbolic curves given for values of $b' > 1$. As $b' > 1 \rightarrow 2$ (equating to the Arps condition $b > 0 \rightarrow 1$). The duration of the coda decline increases, in effect allowing for longer duration processes to supersede shorter duration processes.

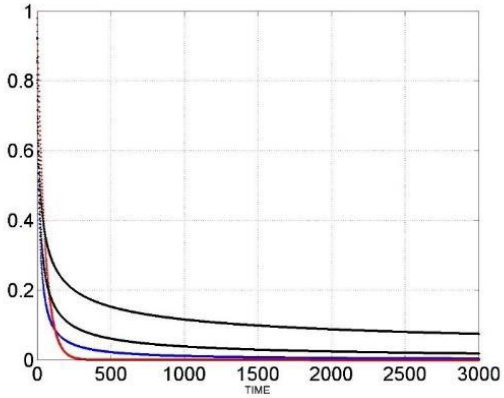

Fig 11 – A range of well production elapsed time decline curves. Red denotes exponential decline involving a single scale process, exp(-t/t9). Blue and black traces denote a generic multi-scale process , $1/(1 + b't/t_0)^{1/b'}$. For parameter b' = 1, the multi-scale process reduces to an exponential decline as shown in blue. For parameter b' > 1 → 2, the decline curves grow in duration as given by black traces.

Utah project coda decline data of Fig 12 illustrates that deep sensor coda wave declines require the presence of both shorter and longer duration processes. Fig 13 summarises the distribution of *b'* over 121 Utah project Meqs. The same plots hold for Helsinki deep sensor data.

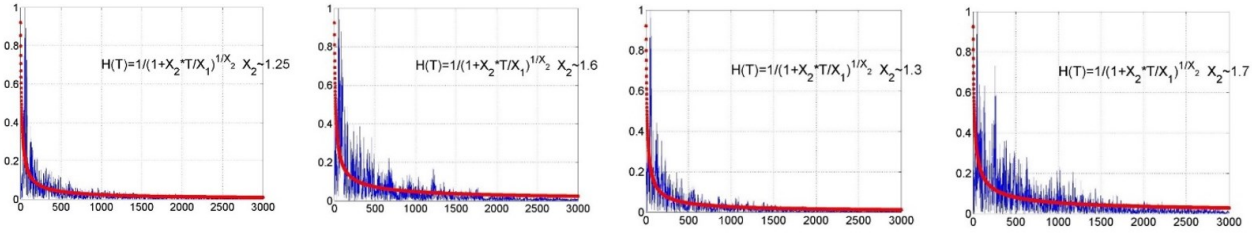

Fig 12 – Quartet of UtahForge Meq coda wave decline curves fit to hyperbolic curves with specific values of parameter b' (here denoted X_2). In line with 121 such coda decline fits, the present 4 coda shown above declines require values of b' > 1, indicating the need for both short- and long-scale coda wave scattering processes.

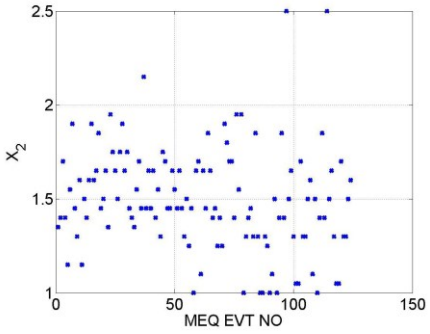

Fig 13 – Distribution of hyperbolic curve b'-= X_2 parameter values. The values equate to Arps' parameter range 0 < IbI < 1. Only a few Meq coda waves with b' ~ 1 decline as fast an exponential as in Fig 3.1. The great majority of Meq coda declines require the presence of longer-term scattering elements to explain their duration. The most frequent value b'~1.5 equates to Arps' typical well flow parameter value b ~ 0.5 [4].

The fundamental multiscale nature of property of the Arps hyperbolic curves is outlined in Fig 14. It is seen that the Arps flow decline analysis is equivalent to the statement that well flow rates decline is a power-law relation to well production. A power-law scaling relation is expressly and inherently multiscale. Such a multiscale relation is given by the ambient crust poro-perm spatial distribution $\kappa(x,y,z) \sim \exp(\alpha\varphi(x,y,z))$ that was unknown to Arps. The power-law scaling of the pink-point porosity distributions in the ambient crust are fundamental to crustal flow heterogeneity with implications for geothermal energy.

Data 1945	$d(Q/(dQ/dt))/dt \sim -b$	(Arps 7)
Solve for time	$Q/(dQ/dt) \sim -bt - a0$	(Arps 8)
Rewrite	$dQ/dt \sim -Q/(bt + a0)$	(Arps 9)
Integrate	$Log(Q/Q0) \sim -1/b \log(1+t/t0)$	
Exponentiate	$Q(t) \sim Q0/(1 + bt/a0)^{1/b}$	(Arps10)
Power-law in Q	$dQ/dt \sim - Q^{1+b}$	(Arps 16)

Power-laws are inherently multiscale

Fig 114– Synopsis of Arps analysis of 1920-30s US oil field production well declines. The declines are tracked by a hyperbolic function (Arps 10) and are due to multiscale flow processes as indicated by the power-law scaling relation (Arps 16).

We thus encounter a crustal reservoir flow expression that explicitly involves a power-law in a physical variable, well flow P. A power-law is inherently scale independent, allowing for many scales to be present in a physical system. If the exponent term $b = 0$, the production decline follows the exponential condition, $dP/dt \sim -P$. Exponential decline is a default case that involves a single scale length. For $b > 0$, the decline involves more scale lengths, thus drawing out production decline to longer times as larger scale length become involved in the decline. Put differently, in multiscale-length flow processes, smaller permeability structures drain faster, leaving larger permeability structures that drain more slowly.

The significance of the hyperbolic decline curves fits is two-fold. First, we see that values of coda wave amplitude decline parameter *b'* vary over the km-scale stimulation crustal volume, indicating that a wide range of scale lengths within the stimulation volume lies behind the high frequency scattering processes that produce the coda declines. Second, the hyperbolic curve formalism applied to reservoir flow properties establish a link to power-law scaling phenomenology that happens to correspond to the multiscale ambient crust poro-permeability distribution $\kappa(x,y,z) \sim \exp(\alpha\varphi(x,y,z))$. The link of coda scattering to crustal flow properties is strengthened by its congruence with the flow decline as in Figs 15-17.

The exponentiated porosity distribution $\varphi(x,y,z)$ comprises volumetric pink-noise fluctuations such that a wellbore spatial sequence in any direction has a Fourier power-law spectral trend that scales inversely with spatial frequency k, $S(k) \sim 1/k$. The pink-noise volumetric distribution is numerically realised in Fig 15 (left). In consequence of the ambient crust poro-permeability distribution, crustal volumes of all sizes from m to km have permeability structures as represented in Fig 15 (right). The larger scale poro-permeability structures in a km-scale crustal volume have the same power-law-scaling two-point spatial correlation function $G(r) \sim 1/r$ as do the Utah and Helsinki stimulation Meqs. It is therefore probable that the Meq dislocation slip source emissions take place in the permeability structures. The same argument applies to smaller (and more numerous) poro-permeability structures that are too small to generate individually detected seismic emissions, and thus become part of the deep crustal background wavefield registered by the Utah and Helsinki) deep sensors.

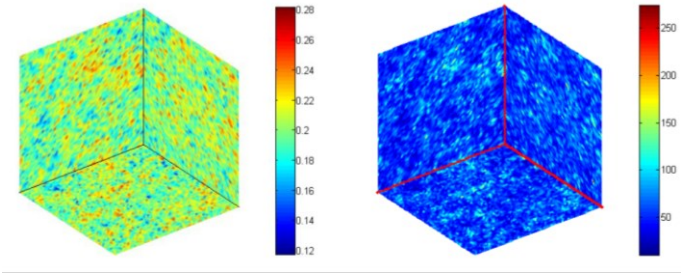

Fig 15 – Numerical realisation of (left) pink-noise porosity volumetric distribution $\varphi(x,y,z)$, and (right) poro-permeability volumetric distribution $\kappa(x,y,z) \sim \exp(\alpha\varphi(x,y,z))$ for parameter $\alpha = 25$ corresponding to the crust-wide empiric 3-4 < $\alpha\underline{\varphi}$ < 5-6 for mean porosity $\underline{\varphi} = 0.2$. The poro-permeability field contains a power-law-scaling range of scattering heterogeneity from m to km scales, and can account for the Meq coda durations in Figs 12-13.

We can translate the Arps drawing out of flow amplitude decline in systems operating over a range of flow-structure scales into the scattering process of coda waves. Progressive removal of high frequencies that are more active per unit time leaves the coda decline to longer wavelengths which encounter fewer scatterers per unit time, hence progressively slowing the coda wave amplitude decline. We thus connect the Arps hyperbolic multiscale crustal flow declines to ambient crust multi-scale-length poro-permeability distributions $\kappa(x,y,z) \sim \exp(\alpha\varphi(x,y,z))$ and thence to Utah and Helsinki EGS stimulation Meq coda wave multi-scale-length declines. The structured randomness of EGS stimulation Meqs is seen in the lognormal distribution of Meq moments and the two-point spatial correlation of Meq pairwise offsets. Fig 16 shows the lognormal moment distributions and the two-point Meq pairwise offset spatial correlation function $G(r) \sim 1/r^p$, $p \sim 1$, fits for the three stages of Utah stimulation conducted in April 2022. Fig 17 outlines the corresponding simulation empirics for the structured randomness of the ambient crust poro-permeability compared with the empirics for unstructured randomness.

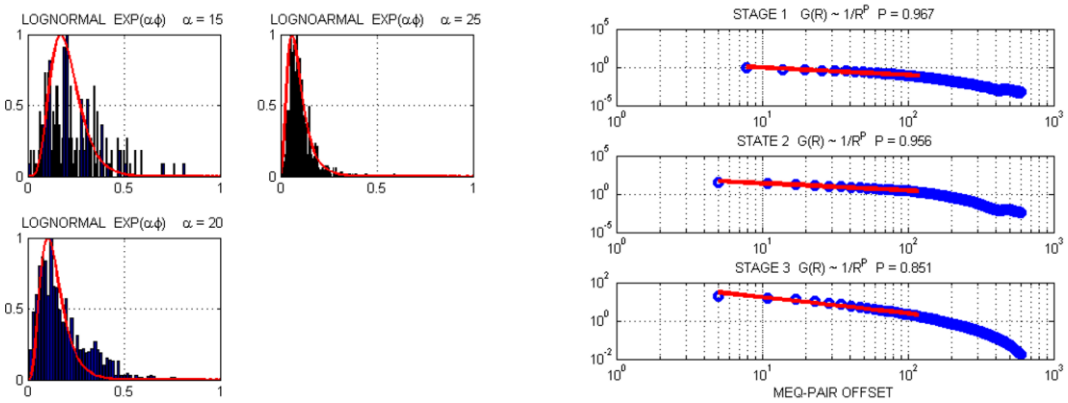

Fig16 -- (Left) Lognormal distributions of Utah project Stage 1-3 Meq moments; red traces are lognormal distribution curves exp(αφ) fit to Meq data for normally distributed porosity distribution $0 < \varphi < 0.3$ with mean value $\underline{\varphi} = 0{,}2$ and α the empirical poro-connectivity parameter. (Right) Log-log plot of two-point spatial correlation distribute of Meq pairwise offset r, with red traces fit to function $G(r) \sim 1r^p$ for $p \sim 1$.

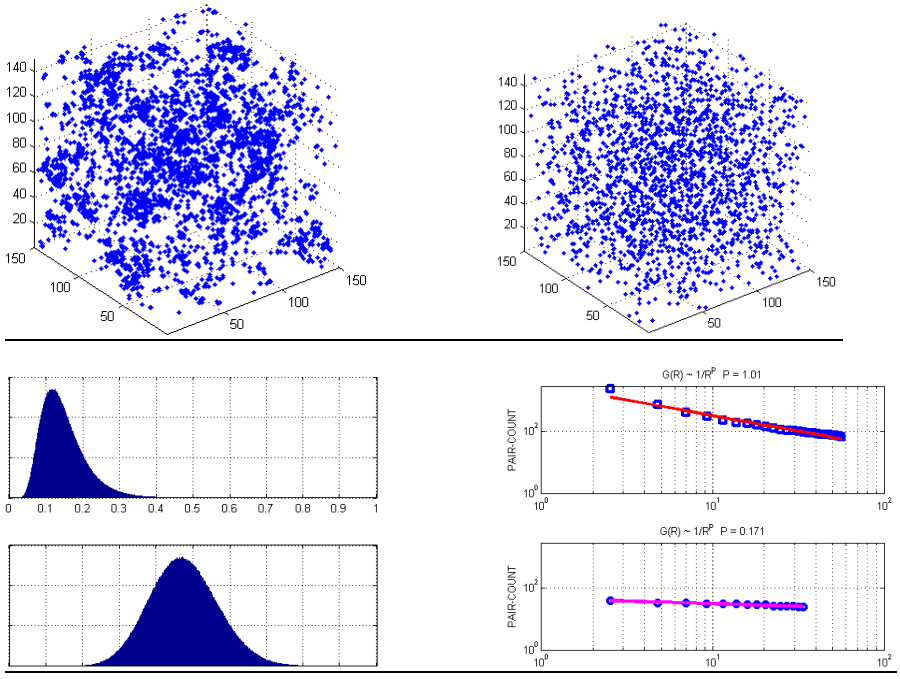

Fig 17 -- (Upper) Spatial distribution of high-value poro-permeability loci for pink-noise structured randomness (left) and white-noise unstructured randomness (right). (Lower Left) Frequency distributions of poro-permeability loci for pink-noise porosity (lognormal above) and white-noise porosity (normal below). (Lower right) Two-point spatial correlation distributions fit to function $G(r) \sim 1/r^p$ for high-value poro-permeability loci for pink-noise porosity with $p \sim 1$ (above) and white-noise porosity with $p \sim 0$ (below).

The observed Utah and Helsinki Meq coda wave amplitude decline empirics are firmly related by hyperbolic curve fitting to multiscale scattering distributions in the ambient crust. The same hyperbolic curve fitting systematics apply to oil field well production declines, implying multiscale flow structure distributions. The ambient crust poro-permeability empiric $\kappa(x,y,z) \sim \exp(\alpha\varphi(x,y,z))$ is explicitly calculatable by construction. The size and spatial correlation distributions of Utah and Helsinki Meqs are congruent with the size and spatial correlation distributions crustal multiscale poro-permeability. We thus assert that observed Utah and Helsinki coda wave multiscale scattering empiric directly originates in the ambient crust poro-permeability structures. There is thus a close and intimate relation between stimulation Meq production and emission which generates scattering

wavefields that carry information about the flow structure of crustal stimulation volumes. The details of this Meq-emission--to-flow-structure relation emerge in the following section.

§3 -- Deep sensor empirics for decaHz stimulation wavefield emissions that can be SET-processed into subsurface flow images

Deep seismic sensor data acquired for the Helsinki and Utah EGS stimulation projects reveal a heretofore unrecognised seismic wavefield that connects ambient crust microseismicity to ambient crust fluid flow structures. In Figs 3-6 we see deep sensor seismic wavefield spectral peaks at kHz and decaHz frequencies While the kHz spectral peaks are directly traceable to stimulation Meq seismic emissions the decaHz spectral peaks are indirectly traceable to residual scattered residual decaHz stimulation seismic wavefields. Figs 12-17 trace the seismic scattering process to the multiscale poro-permeability structures that pervade the ambient crust. We here look at deep sensor direct evidence of decaHz residual scattered wavefields that propagate through the deep sensor array from the Meq stimulation volume to the crustal surface as sketched in Fig 18. Despite the small amplitudes of residual scattered decaHz wavefields, their distribution in time and space can be processed by Seismic Emission Tomography (SET) methods into seismic energy images that represent crustal flow structures.

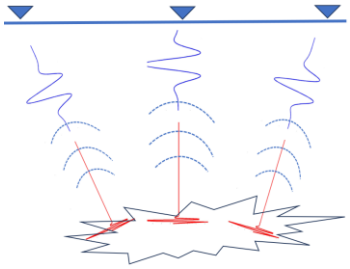

Fig 18 – Schema of SET crustal flow imaging seismic wavefield elements. The irregular shape at bottom represents a subsurface Meq stimulation volume. Such as numerically realised in Figs 15-17. Red waveforms in the stimulation volume represent kHz frequency Meq emissions activated by stimulation fluids. Consecutive dashed curves represent upwards propagating scattered seismic wavefields as seen in in Figs 19-21. Blue waveforms represent the decaHz residual wavefields that reach the surface sensors denoted by inverted triangles. Each Meq source point emits a burst of kHz emission energy which in turn generates its own residual scattered decaHz wavefield that registers on array surface sensors at a source-sensor-specific travel time. SET processing uses the array of travel times returned by the array of surface sensors to spatially locate the position of the Meq emissions as pictured in Fig 22 for SET data acquired at the Newberry volcano geothermal site in Oregon.

While the most evident feature of the decaHz background wavefield is its Fig 3 spectral peak in the single channel of Utah project strain wavefield data, the wavefield scattering origin process is more directly seen in the Figs-12-13 strain motion coda wave amplitude decline empirics. The physical properties of the scattered wavefield is still more directly seen in the multisensory Helsinki project array-sensor velocity data of Figs 19-21.

The Helsinki decaHz scattered background wavefield sample in Fig 19 is the residual product of seismic waves traveling over 4km travel paths from the source stimulation volume at 6km depth to the 12-module sensor array at depths 2-2.5km depth directly above the stimulation volume [11]. The deep sensor array comprises 6 modules at 10m spacing below 6 modules at 75m spacing, vertically extending over 500m of crust. Fig 19 shows two traces of 900 velocity amplitude data sampled at half-msec intervals The chief wavefield frequency is ~ 13 cycles per half-second or ~25Hz, with hHz fluctuations superposed. Most notably, the two traces are clearly strongly coherent on array sensors 10 meters apart. The background wavefield is thus seen to be a form of structured noise as might arise from scattering of a single propagating wavefield rather than unstructured noise due to a large number of scattered waves from multiple sources. The spectral signature of the sample wavefield is seen in Fig 5. The equivalent Utah project scattered wavefield spectra seem in Fig 3.

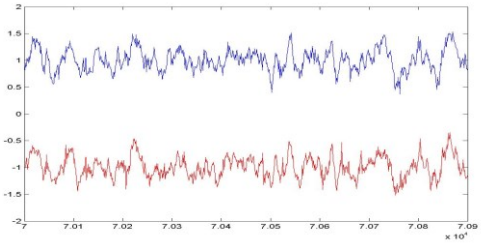

Fig 19 – Structured noise records for 2.5km deep Helsinki background wavefield velocity sensors 10m apart. The low frequency wave motion is visibly in phase across the sensor interval, ruling out a spurious sensor noise origin for the low frequency spectral component of background wavefields such as seen in Fig 4. A high degree of low frequency commonality and a lesser degree of high frequency cross-correlation commonality are established in Fig 20.

The Fig 19 deep sensor decaHz scattered background wavefield coherence across adjacent sensors is quantified in Fig 20 across the entire vertical deep sensor array. High- and low-pass filtering 20-second intervals of Fig 19-like velocity traces, Fig 20 cross-correlates successive array sensor traces against the bottom-most trace for low-pass (left) and high-pass (right) data. The high-pass data correlates significantly across 10m sensor offsets but loses coherence at 75m sensor offsets as high-frequency scattering alters the progressing wavefield. The low-pass data retains, however, a significant degree of waveform coherence across the entire sensor array as the number of scattering encounters decreases for the long wavelengths.

Key to Fig 20 coherence systematics is the time-migration of peak coherence lags with increasing sensor offset. While the peak coherence lag is evidence for the high-pass data for 10m sensor offsets, we can quantify the lowpass data migration rate as given by the red circles above the peak coherence. The low-pass lag migration rates are amplified inf Fig 21.

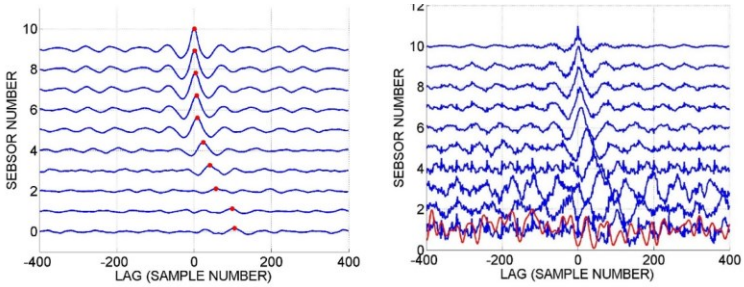

Fig 20 – (Left/Right) Cross-correlated 10-second records of low/high frequency background wavefield components of Helsinki deep sensor data for successive sensor offset intervals. Upper trace intervals are 10m; lower trace intervals are 75m. The cross-correlation peaks for low frequency wavefields marked by red dots show the background wavefield motion at successive sensors is progressively delayed as the background wavefield ascends through the wellbore sensor array. The high frequency correlation at 76m offsets descend into uncorrelated noise as illustrated by the red trace.

Fig 21 expands the Fig 20 (left) cross-sensor correlation traces between successive Helsinki deep sensor array modules to quantify the temporal moveout of the sensor cross-correlation peaks as the decaHz scattering residual background wavefield passes through the sensor array. The migrating peak-coherence lag corresponds to the Fig 19 sample scattering residual wavefield ascending vertically though the Helsinki sensor array at P-wave speed 5.5km/s. We thus establish through multi-sensor cross-coherence of the Fig 19 deep sensor decaHz sensor traces the systematic presence of EGS stimulation seismic emission wavefields that can register EGS stimulation Meq event occurrence on decaHz-passband surface sensors.

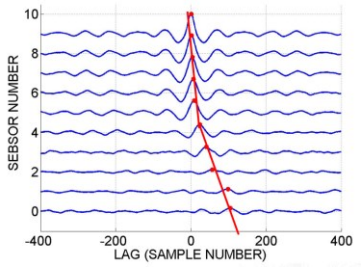

Fig 21 – Expanded display of Fig 20 progressive delays in sensor-sensor peak cross-correlation as low frequency background wavefield ascends through the Helsinki wellbore sensor array. Peak sensor correlation delays of upper traces increase in 2msec steps corresponding to 10m sensor intervals, while lower trace delays increase in 15msec steps for the 75m sensor intervals. Correlation lags are in half-msec steps; the total elapsed delay of ~60msec corresponds to traversing the ~350m array length at ~5.5m/msec P-wave seismic wave speed.

The utility of Fig 18-21 decaHz residual scattered wavefields is illustrated in Fig 22. Pictured is a 2.5km^2 horizontal plane section of SET-processed seismic energy emission coherence at km-depth below the crustal surface at the Newberry volcanic geothermal system in Oregon, USA. Warm/cool colours indicate areas of active/inactive seismic energy emission that are logically are sites of active/inactive convective fluid flow. The spatially erratic distribution of seismic energy emission coherence is expected from the ambient crust poro-permeability distribution $\kappa(x,y,z) \sim \exp(\alpha\varphi(x,y,z))$ displays in Fig 15 (right) and Fig 17 (upper left). Production well drilling for access to active convective fluid flow structures would be directed towards the warm colour locations and way from cool colour locations. It is evident that warm colour areas are outnumbered by cool colour area in approximately the ratio 80/20, corresponding to the Pareto 80/20 distribution of well productivity attested oil/gas well production data [31]. The Pareto 80/20 distribution says that 80% of crustal reservoir well pay from 20% of wells, while 20% of pay comes from 80% of wells. While oil/gas production wells generally pay for themselves over a sufficient operational lifetime, 80% of geothermal production wells are unrecoverable/sunk costs. Flow structure images such as Fig 22 can eliminate the 80% of unproductive geothermal well drilling cost.

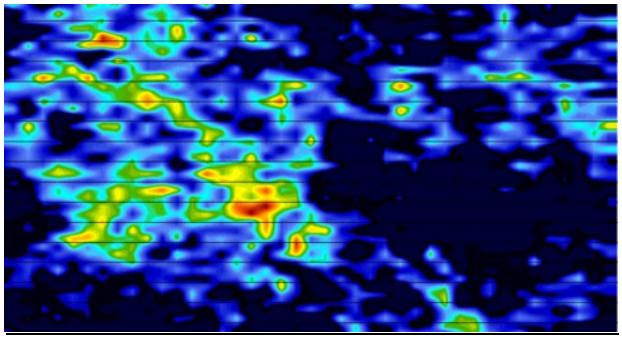

Fig 22 – A 2.5km^2 horizontal plane section of SET-processed seismic energy emission coherence at 1km depth below the crustal surface at the Newberry volcanic geothermal system in Oregon, USA. Warm/cool colours mark areas of high/low seismic emission activity that correspond to areas of high/low fluid flow activity. Drill geothermal production wells only in warm colour areas eliminates much of convective geothermal production well drilling costs.

Summary and Conclusions

Km-deep seismic sensor data acquired at two EGS stimulation sites reveal the considerable short-coming of surface seismic sensor data. EGS stimulation processes at 1.5km and 6km depths are revealed by seismic sensors at 1.5-2.5 km depth to (i) proceed at kHz frequencies, an order of magnitude higher than supposed from standard frequency-band-limited surface seismic monitoring networks; and (ii) systematic seismic wave scattering at multiscale crustal poro-permeability structures whose presence was demonstrated 80 years ago by the Arps analysis of production well flow declines. Systematic multiscale scattering of kHz Meq emissions from EGS stimulation volumes is seen in deep sensor data to generate a decaHz background wavefield that can be recorded by standard surface seismic sensors. However, because of its low amplitude and disseminated nature, this decaHz residual scattered stimulation wavefield has not been recognised to exist until its presence was revealed by deep sensor EGS stimulation data.

The decaHz residual scattered stimulation wavefield is most directly seen in the Fig 21 cross-sensor coherence traces recorded by a 2.5km deep wellbore sensor array. The decaHz residual scattered wavefield is more obviously attested by deep sensor spectral data shown in Figs 3 and 5. With its physical presence established by deep sensor data, we can now identify its existence in terms of more specialised multisensory data processing. The low amplitude disseminated background wavefield emission from stimulated crustal volumes has in fact been routinely detected indirectly by Seismic Emission Tomographic (SET) processing of surface seismic array data acquired during hydrocarbon-bearing shale formation stimulation recovery [21-23].

The utility of the SET processing of the decaHz residual scattered stimulation background wavefield is illustrated by Fig 22. While the more evident kHz stimulation process seismic emissions have been recorded by band-limited surface sensors, prior to deep seismic sensor stimulation Meq recordings there has been no recognition of the essential physical processes involved in their production. We here rectify this long-standing misrepresentation of stimulation Meq production by showing that (i) the

Meqs are kHz processes essentially invisible to surface sensors, (ii) the deep-sensor-visible kHz processes are intimately related to ambient crust poro-permeability structures, and (iii) the previously unknown scattered residual decaHz wavefields emitted by Meq stimulation processes are visible to surface seismic sensors and hence can be detected by SET processing methods. As per Fig 22, applying the proven SET imaging technique to convective geothermal systems can improve the production well drilling outcomes and can effectively monitor EGS stimulation volumes in order to efficiently connect injector wells to production wells.

References

[1] Gringarten AC, Witherspoon PA & Ohnishi Y (1975) Theory of heat extraction from fractured hot dry rock, *Journal of Geophysical Research*, 1120-1124.

[2] Wunder R & Murphy H (1978) Singly and multiply fractured hot dry rock reservoirs, Los Alamos National Laboratory Report, LA-
7219-MS, UC-66a, 1-15.

[3] Tester JW et al (2006) The Future of Geothermal Energy, Impact of Enhanced Geothermal Systems (EGS) on the United States in
the 21st Century, http://geothermal.inel.gov.

[4] Sutter D, Fox DB, Anderson BJ, Koch DL, Von Rohr PF, Tester JW (2011) Recovery in a Model EGS Fractured Reservoir, 36th
Workshop on Geothermal Reservoir Engineering, Stanford Geothermal Program Workshop Report SGP-TR-191

[5] Zimmerman RW & Bodvarsson G (1994) Hydraulic conductivity in rock fractures, LBL-35976 UC-800;

[6] Sisavath S, Al-Yaarubi A, Pain CC & Zimmerman RW (2003) A simple model for deviations from the cubic law for a fracture undergoing dilation or closure. PAGEOPH 160, 1009–1022;

[7] Zimmerman RW (2012) The history and role of the cubic law for fluid flow in fractured rocks. In Proceedings of the Session H071 Dynamics of Fluids and Transport in Fractured Porous Media, San Francisco, CA, USA, 3–7 December 2012.

[8] Gibbs JF, Healy JH, Raleigh CB & Coakley J (1973) Seismicity in the Rangely, Colorado, Area: 1962-1970, Bulletin Seismological Society of America 63.

[9] Aki K & Richards PG (1980) *Quantitative Seismology, Theory and Methods*, Chap 14,. ISBN 0 7167 1058 7 (Vol. I), 0 7167 1059 5 (Vol. II)

[10] Aki, K and P. Richards Quantitative Seismology, (2009), Chap 12 2nd Edition University Science Books ISBN-10. 1891389637 · ISBN-13. 978-1891389634·

[11] Kwiatek, G., T. Saarno, T. Ader, F. Bluemle, M. Bohnhoff, M. Chendorain, G. Dresen, P. Heikkinen, I. Kukkonen, P. Leary, M. Leonhardt, P. Malin, P. Martínez-Garzón, K. Passmore, P. Passmore, S. Valenzuela, C. Wollin (2019) Controlling fluid-induced seismicity during a 6.1-km-deep geothermal stimulation in Finland. Sci. Adv. 5, eaav7224

[12] Lei Q, Latham J-P & Tsang C-F (2017) The use of discrete fracture networks for modelling coupled geomechanical and hydrological behaviour of fractured rocks, Computers and Geotechnics 85 (2017); http://dx.doi.org/10.1016/j.compgeo.2016.12.024.

[13] Alghalandis YF, Elmo D & Eberhardt E (2017) Similarity Analysis of Discrete Fracture Networks, arXiv:1711.05257.

[14] Elmo D, Rogers S, Stead D & Eberhardt E (2014) Discrete Fracture Network approach to characterise rock mass fragmentation and implications for geomechanical upscaling, Journal Mining Technology, Transactions of the Institutions of Mining and Metallurgy, Vol 123;doi.org/10.1179/1743286314Y.0000000064.

[15] Arps JJ (1945) Analysis of Decline Curves, SPE-945228-G Arps Original 1945

[16] Geiser P, Vermilye J, Scammell R & Roecker S (2006) Seismic used to directly map reservoir permeability fields, Oil & Gas Journal 104, No. 46

[17] Geiser P, Lacazette A & Vermilye J (2012) Beyond 'dots in a box': an empirical view of reservoir permeability with tomographic fracture imaging, First Break, Volume 30.

[18] Geiser P & Leary P (2014) Tomographic Fracture Imaging (TFI): Direct 5D Mapping of Transmissive Fracture/fault Zones Using Seismic Emission Tomography (SET), 39th Workshop on Geothermal Reservoir Engineering Stanford University,, 2014 SGP-TR-202

[19] Leary P & Malin P (2023) Permeability-specific Meq spatial correlation systematics for UtahForge Well 16A(78)-32 stimulation stages 1-3, Proceedings 49th Stanford Geothermal Workshop; SGP-TR-224 1;

[20] Malin PE, Leary PC, Cathles LM & Barton CC (2020) Observational and critical state physics descriptions of long-range flow structures, *Geosciences* 2020, *10*(2), 50; https://doi.org/10.3390/geosciences10020050

[21] P Leary, P Malin, G Saunders & C Sicking (2020) Seismic Imaging of Convective Geothermal Flow Systems to Increase Well Productivity Journal of Energy and Power Technology volume 2, issue 3 doi:10.21926/jept.2003012;

[22] P Leary & P Malin (2021) Crustal Reservoir Flow Simulation for Long-Range Spatially-Correlated Random Poroperm Media, Journal of Energy and Power Technology, volume 3, issue 1 doi:10.21926/jept.2101013

[23] PC Leary & PE Malin (2022) Observation of Meq HHz Coda in the Ambient Crust -- Implications for Surface Seismic Array Flow Imaging, 47th Workshop on Geothermal Reservoir Engineering Stanford University, SGP-TR-223.

[24] Whidden K, Petersen G & Pankow K (2023) Seismic Monitoring of the 2022 Utah FORGE Stimulation: View from the Surface, 48th Workshop on Geothermal Reservoir Engineering Stanford University, SGP-TR-224.

[25] Malin P & Leary P (2023) Haskell waveform modeling of EGS stimulation Meqs as slow ruptures within ambient crust permeability structures, Proceedings 49th Stanford Geothermal Workshop; SGP-TR-224.

[26] Haskell NA (1969) Elastic displacements in the near-field of a propagating fault, Bull. Seisin. Soc. Am., 59, 865-908.

[27] Bracewell RN (1978). *The Fourier Transform*. McGraw-Hill. New York.

[28] Hanks TC and Kanamori H (1979) A Moment Magnitude Scale, *Journal of Geophysical Research*, **84** (B5): 2348–2350

[29] Frankel A and Clayton RW (1986) **Fi**nite difference simulations of seismic scattering: Implications for the propagation of short-period seismic waves in the crust and models of crustal heterogeneity. doi.org/10.1029/JB091iB06p06465

[30] Chernov LA (1960) Wave Propagation in a Random Medium, Trans R. A. Silverman, Journal of Applied Mechanics, Dover Publications 2017

[31] all-years-states_useia.xls (2009) U.S. Energy Information Administration (EIA)